Available online at www.sciencedirect.com
ScienceDirect
International Journal of Heat and Mass Transfer 51 (2008) 2433–2443
International Journal of HEAT and MASS TRANSFER
www.elsevier.com/locate/ijhmt

Numerical simulation of a fountain flow on nonstaggered Cartesian grid system

Shong-Leih Lee *, Wei-Ching Liao

Department of Power Mechanical Engineering, National Tsing Hua University, Hsinchu 30013, Taiwan

Received 25 August 2006; received in revised form 9 April 2007
Available online 25 October 2007

Abstract

A liquid–air fountain flow due to the downward motion of a rectangular sleeve over a stationary piston is studied in the paper. Two-dimensional incompressible laminar flows are assumed to prevail in both air and liquid regions. A single set of governing equations over the entire physical domain including the liquid, the air, and the liquid–air interface (free surface) is solved with the extended weighting function scheme and the NAPPLE (nonstaggered APPLE) algorithm on a fixed nonstaggered Cartesian grid system. To ensure the required dynamic contact angle, the liquid meniscus near the sleeve wall is corrected by solving the force balance equation with the geometry method. This is equivalent to introducing a slip condition at the contact line, and thus successfully removes the stress singularity. Steady state solution of the velocity and the pressure as well as the shape of the free surface is obtained. The numerical result evidences the existence of a toroidal-like motion on the free surface postulated by Dussan [E.B. Dussan V., Immiscible liquid displacement in a capillary tube: the moving contact line, AIChE J. 23 (1977) 131–133], although it is quite weak and thin. The resulting free surface profile agrees with the existing experimental observation excellently. Influence of the piston on the flow is discussed.

Keywords: Fountain flow; Nonstaggered Cartesian grid system; Dynamic contact angle; Piston effect

1. Introduction

The problem dealing with displacement of one fluid by another immiscible fluid is encountered in nature and many industrial applications such as coating operation, oil recovery, and mold filling process. It is well-known that a fluid entering the region near the advancing interface of two immiscible fluids in a narrow channel decelerates in the flow direction and acquires a transverse velocity to spill outward the wall. Such a flow characteristic was coined with the term "fountain effect" by Rose [1].

Numerical simulation for the fountain flow is a challenging problem because of three principal numerical difficulties. First, there is a stress singularity at the contact line due to the no-slip condition on the wall for both fluids. Second, the free surface profile having an irregular shape is not known. Third, the capillary force arising from the curvature of the free surface and the dynamic contact angle should be precisely evaluated. To remove the stress singularity at the contact line, Dussan V. and co-worker [2,3] and Cox [4] postulated that there should be a region of size l_s around the contact line in which the no-slip condition breaks down. However, the molecular dynamic simulations [5,6] demonstrate that the slipping length is of the order $l_s \approx 0.001\mu m$ for smooth solid walls having smoothness on the molecular scale. Similarly, the "effective" slipping length should be on the order of the typical period of the random undulations for rough walls [7,8]. Unfortunately, it is not practical to implement such a tiny slipping length in the numerical simulation for the flow field.

Behrens et al. [9] proposed a rolling model for the advancement of the free surface. However, the rolling model poses to an oscillating advancement for the contact line. Moreover, there is a mass loss on the wall. Similar

* Corresponding author. Tel./fax: +886 3572 8230.
E-mail address: sllee@pme.nthu.edu.tw (S.-L. Lee).

0017-9310/$ - see front matter © 2007 Elsevier Ltd. All rights reserved.
doi:10.1016/j.ijheatmasstransfer.2007.08.030

Nomenclature

$a_W, a_E, a_S, a_N, a_P, a_R$	weighting factors of the finite difference Eq. (13a)
Bo	Bond number, $(\rho_l - \rho_a)gL^2\gamma$
Ca	Capillary number, $\mu_l U_c/\gamma$
Fr	Froude number, $U_c/\sqrt{gL}$
$h(x,\tau)$	free surface profile
L	inner width of the rectangular sleeve, Fig. 1
P_{ref}	reference pressure, N m^{-2}
p	dimensionless pressure, $(P - P_{ref})/\rho_l U_c^2$
$\hat{p}$	dimensionless pressure, Eq. (4)
Re	Reynolds number, $\rho_l U_c L/\mu_l$
u, v	dimensionless velocity, U/U_c and V/U_c
U_c	reference velocity
V_{wall}	moving speed of the sleeve, m s^{-1}
v_n	dimensionless normal velocity on the free surface
w_f	weighting function, $z/(1-\exp(-z))$
$\hat{w}_f$	extended weighting function, Eq. (17)
(x,y)	coordinate system
x_{joint}	a location near the wall, Fig. 4
y_{ref}	reference altitude
z	grid Peclet number, Eq. (13b)

Greek symbols

γ	surface tension, N m^{-1}
$\Delta x, \Delta y$	grid meshes
$\Delta\tau$	virtual time step
θ_D	dynamic contact angle
κ	curvature of the free surface
μ^*	dimensionless viscosity, Eq. (6)
ρ^*	dimensionless density, Eq. (5)
σ_{nn}	normal stress on free surface
τ	virtual time
ψ	stream function, Eq. (40)

Subscripts

a	air
l	liquid

result was obtained by Kim et al. [10] when the rolling model and the VOF (volume-of-fluid) scheme were used to track the moving free surface. For consideration of the mass conservation on the wall, Mavridis et al. [11] modified the rolling model by imposing the kinematic condition with the no-slip hypothesis at the contact line. When applied to a start-up free surface flow, however, the modified rolling model [11] does not allow the contact line to move until the contact angle increases from the static contact angle to 180°. As a result, the dynamic contact angle is always 180° despite of the capillary number. This does not seem physically realistic because the dynamic contact angle should be a strong function of the capillary number as well-recognized in the literature [12].

In an early experiment on the displacement of mineral oil by glycerine in a Plexiglas circular tube of 6.35 mm inner diameter, Dussan V. [13] observed that the glycerine underwent the familiar fountain flow, while the mineral oil contained a toroidal-like motion in a region adjacent to the interface. Based on the finding, Dussan V. [13] postulated the existence of a toroidal-like motion in the region directly above and immediately adjacent to the interface of two immiscible fluids.

The problem of injection mold filling is one of the important applications of the fountain flow in liquid–air system. The literature in the area (e.g. [14–19]) seems restricted to problems without capillary force and body force. Moreover, the inlet velocity is assumed to have a fully developed parabolic profile. Such investigations closure the problem by imposing some "boundary conditions" on the free surface, and thus cannot observe the flow field in the air region. The purpose of the present work is to re-examine the fountain flow in liquid–air system by solving velocity and pressure in both liquid and air regions on a fixed nonstaggered Cartesian grid system. The free surface profile in the wall region is corrected with the required dynamic contact angle to remove the stress singularity at the contact line. In this connection, both capillary force and body force should be taken into account especially in the wall region.

2. Theoretical analysis

In their experiment, Coyle et al. [20] used a constant-speed motor to lower a transparent acrylic sleeve over a stationary aluminum piston that rested on the floor. A Newtonian silicon oil was poured into the region above the aluminum piston with the acrylic sleeve in the position shown in Fig. 1. The inner cross-section of the sleeve was $2L \times 2W = 0.038\ \text{m} \times 0.114\ \text{m}$. The sleeve had a moving speed of only $V_{wall} = 0.002$ m/s while its length was 1.016 m such that the steady-state flow was reached. Coyle et al. [20] found that the flow was essentially two-dimensional when viewed from the narrow side (see Fig. 1). In the present study, this same flow configuration is formulated by

$$\frac{\partial u}{\partial x} + \frac{\partial v}{\partial y} = 0 \tag{1}$$

$$\rho^* Re\left(\frac{\partial u}{\partial \tau} + u\frac{\partial u}{\partial x} + v\frac{\partial u}{\partial y}\right) = -\frac{\partial \hat{p}}{\partial x} + \frac{\partial}{\partial x}\left(\mu^*\frac{\partial u}{\partial x}\right) + \frac{\partial}{\partial y}\left(\mu^*\frac{\partial u}{\partial y}\right) \tag{2}$$

$$\rho^* Re\left(\frac{\partial v}{\partial \tau} + u\frac{\partial v}{\partial x} + v\frac{\partial v}{\partial y}\right) = -\frac{\partial \hat{p}}{\partial y} + \frac{\partial}{\partial x}\left(\mu^*\frac{\partial v}{\partial x}\right) + \frac{\partial}{\partial y}\left(\mu^*\frac{\partial v}{\partial y}\right) \tag{3}$$

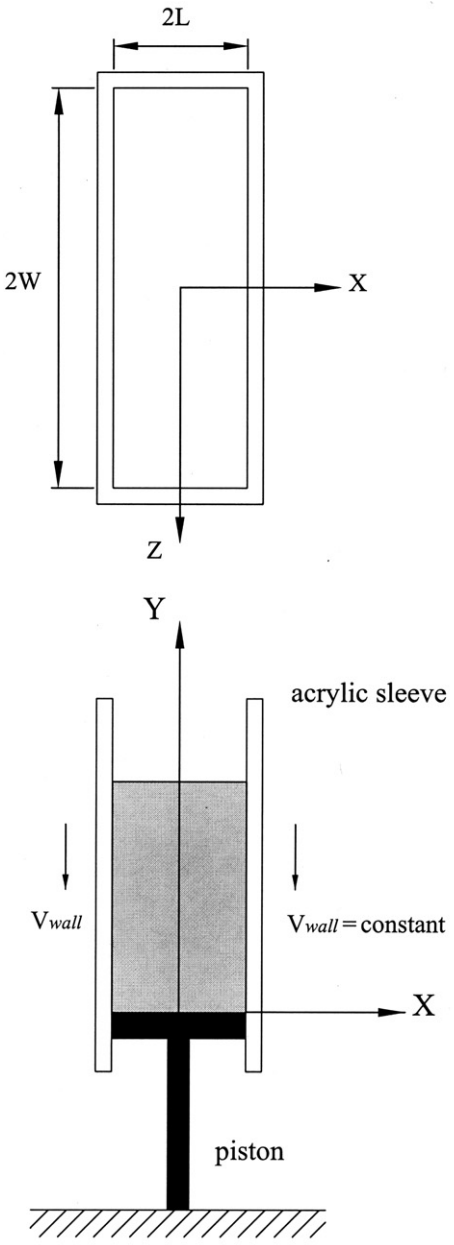

Fig. 1. Flow configuration of the problem.

based on the following dimensionless transformation:

$$x = X/L, \quad y = Y/L, \quad u = U/U_c,$$
$$v = V/U_c, \quad \tau = (U_c/L)t$$
$$Re = \frac{\rho_l U_c L}{\mu_l}, \quad Fr = \frac{U_c}{\sqrt{gL}}, \rho^* = \rho/\rho_l, \mu^* = \mu/\mu_l$$
$$p = \frac{P - P_{\text{ref}}}{\rho_l U_c^2}, \qquad \hat{p} = \begin{cases} Re(p + Fr^{-2}(y - y_{\text{ref}})) & \text{in liquid} \\ Re\left(p + \frac{\rho_a}{\rho_l} Fr^{-2}(y - y_{\text{ref}})\right) & \text{in air} \end{cases} \tag{4}$$

where $U_c = V_{\text{wall}}$ is the reference velocity. The reference altitude y_{ref} is to be defined. Mathematically, the dimensionless density ρ^* and viscosity μ^* are step functions across the free surface. They have the value of unity in the liquid region and jump to another constant in the air region, i.e.

$$\rho^* = \begin{cases} 1 & \text{in liquid} \\ \rho_a/\rho_l & \text{in air} \end{cases} \tag{5}$$

$$\mu^* = \begin{cases} 1 & \text{in liquid} \\ \mu_a/\mu_l & \text{in air} \end{cases} \tag{6}$$

where the subscripts 'a' and 'l' denote, respectively, the properties of the air and the liquid. Under this particular formulation, the "free surface" is regarded as an internal boundary of the physical domain, and thus no additional treatment is needed for the shear stress on the free surface.

The pressure jump across the free surface is expressible as the force balance equation [21,22]

$$p_l - p_a = -\frac{1}{Re}\left(\frac{\kappa}{Ca} - (\sigma_{nn})_l + \left(\frac{\mu_a}{\mu_l}\right)(\sigma_{nn})_a\right) \tag{7a}$$

$$Ca = \frac{\mu U_c}{\gamma}, \quad \sigma_{nn} = 2\frac{\partial v_n}{\partial n}, \quad \kappa = \frac{h''}{(1 + h'^2)^{1.5}} \tag{7b}$$

where Ca is the capillary number, and γ is the surface tension. The curvature κ (normalized by L^{-1}) is positive for concave liquid meniscus, while $y = h(x, \tau)$ represents the free surface. The primes in Eq. (7b) stand for the partial differentiation with respect to x. Because both characteristic velocity and characteristic length are small, the normal stress σ_{nn} on the free surface is negligible as compared to the capillary force and the body force in the present case. For simplicity, the reference altitude is defined as $y_{\text{ref}} = 0$. Hence, Eq. (7a) reduces to

$$\hat{p}_l - \hat{p}_a = \frac{1}{Ca}(Boh - \kappa) \tag{8}$$

where the Bond number is defined as

$$Bo = \frac{(\rho_l - \rho_a)gL^2}{\gamma} \tag{9}$$

In the present study, the mean depth of the liquid $\bar{h}$ is less than 4. Thus, it is adequate to employ the region $0 \leqslant x \leqslant 1$ and $0 \leqslant y \leqslant 5$ as the computational domain. The associated boundary conditions are

$$u(0,y,\tau) = 0, \quad \partial v(0,y,\tau)/\partial x = 0, \quad u(1,y,\tau) = 0,$$
$$v(1,y,\tau) = -1$$
$$u(x,0,\tau) = 0, \quad v(x,0,\tau) = 0, \; u(x,5,\tau) = 0, \quad \partial v(x,5,\tau)/\partial y = 0 \tag{10}$$

On the imaginary plane $y = 5$, the pressure is assumed to be the ambient pressure P_∞ such that $p(x, 5, \tau) = 0$ and

$$\hat{p}_a(x,5,\tau) = 5\frac{\rho_a}{\rho_l}\frac{Re}{Fr^2} = 5\frac{\rho_a}{\rho_l - \rho_a}\frac{Bo}{Ca} \tag{11}$$

if the reference pressure is assigned as $P_{\text{ref}} = P_\infty$.

3. Numerical procedure

The governing equation (11), the force balance Eq. (8), the associated boundary conditions (10), and the pressure

level (11) constitute a problem of partial differential equations. In the present study, the numerical procedure is performed on a uniform Cartesian grid system (x_i, y_j), i.e.

$$x_i = (i-1)\Delta x \qquad y_j = (j-1)\Delta y \tag{12}$$

with square meshes $\Delta x = \Delta y$. For convenience, let the grid point (x_i, y_j) be represented by P while its four neighbors (x_{i-1}, y_j), (x_{i+1}, y_j), (x_i, y_{j-1}), (x_i, y_{j+1}) be denoted by the conventional notation W, E, S, N, respectively. In case all of the five points are located in the same phase (liquid or air), the conventional weighting function scheme [23] is employed to discretize the momentum equation (2). The resulting algebraic equation is expressible as

$$a_W u_{i-1,j} + a_E u_{i+1,j} + a_S u_{i,j-1} + a_N u_{i,j+1} + a_P u_{i,j} = a_R + \frac{\partial \hat{p}}{\partial x} \tag{13a}$$

$$a_W = \frac{\mu^* w_f(z_{x,i-1})}{(\Delta x)^2}, \quad a_E = \frac{\mu^* w_f(-z_{x,i})}{(\Delta x)^2}$$
$$a_S = \frac{\mu^* w_f(z_{y,j-1})}{(\Delta y)^2}, \quad a_N = \frac{\mu^* w_f(-z_{y,j})}{(\Delta y)^2}$$
$$a_P = -(a_W + a_E + a_S + a_N) - \frac{Re\ \rho^*}{\Delta \tau}, \quad a_R = -\left(\frac{Re\ \rho^*}{\Delta \tau}\right) u_0$$
$$w_f(z) = \frac{z}{1-\exp(-z)}, \quad z_{x,i} = Re\ \bar{u}\left(\frac{\rho^*}{\mu^*}\right)\Delta x,$$
$$z_{y,j} = Re\ \bar{v}\left(\frac{\rho^*}{\mu^*}\right)\Delta y \tag{13b}$$

where u_0 denotes the velocity u at the previous time $\tau - \Delta\tau$, and $\bar{u}$ and $\bar{v}$ are the average velocities in the intervals $[x_i, x_{i+1}]$ and $[y_j, y_{j+1}]$, respectively. Eq. (3) can be treated similarly.

As observable from Eq. (13), the pressure gradient ($\partial\hat{p}/\partial x$ and $\partial\hat{p}/\partial y$) is proportional to the viscosity μ^* for a low Reynolds number free surface flow such as the present case ($z \approx 0$ and $w_f(z) \approx 1$). This implies a negligible variation in the air pressure $\hat{p}_a(x, h, \tau)$ as compared to the other terms in the right-hand-side of Eq. (8) if $\mu_a/\mu_l \leqslant 1$ and $\rho_a/\rho_l \leqslant 1$. Under such a situation, Eq. (8) reduces to

$$\hat{p}_l = \frac{1}{Ca}(Boh - \kappa) \tag{14}$$

To properly handle the step functions (5) and (6) when the computational cell covers both liquid and air regions including the free surface, the extended weighting function scheme [21] is employed. Suppose the free surface interests the segment $[x_i, x_{i+1}]$ at $x = x_s$ such that the point $P(x_i, y_j)$ and three of its neighbors W, S, N are located in the liquid region while the point $E(x_{i+1}, y_j)$ is in the air region. Applying the integration scheme [24], one has

$$a_E = \left(\Delta x \int_{x_i}^{x_{i+1}} \frac{1}{\mu^*} \exp\left(\int_{x_i}^{x} Re\ u \frac{\rho^*}{\mu^*} dx\right) dx\right)^{-1} \tag{15}$$

Next, integrate Eq. (15) piece by piece over the two subintervals $[x_i, x_s]$ and $[x_s, x_{i+1}]$ to yield the extended weighting function scheme [21]

$$a_E = \frac{\hat{w}_f\left(-z_1, -z_2 \middle| 1, \frac{\rho_a}{\rho_l}, 1, \frac{\mu_a}{\mu_l}\right)}{(\Delta x)^2} \tag{16}$$

where

$$z_1 = Re\bar{u}\Delta x s, \quad z_2 = Re\bar{u}\Delta x \frac{\rho_a \mu_l}{\rho_l \mu_a}(1-s), \quad s = \frac{x_s - x_i}{\Delta x}$$
$$\hat{w}_f(\alpha, \beta | a_1, a_2, b_1, b_2) = \frac{a_2 b_1 \alpha + a_1 b_2 \beta}{a_2(1-\exp(-\alpha)) + a_1(1-\exp(-\beta))\exp(-\alpha)} \tag{17}$$

A general formulation of the extended weighting function scheme for all possible situations can be found in ref. [21]. It can be verified from Eq. (17) that the weighting factor (16) reduces to the counterpart in Eq. (13b) when the interval $[x_i, x_{i+1}]$ contains only a single phase fluid, i.e.

$$a_E = \frac{w_f(-z_{x,i})}{(\Delta x)^2} \quad \text{and} \quad z_{x,i} = z_1 \quad \text{if } s = 1 \tag{18a}$$

$$a_E = \frac{\mu_a}{\mu_l}\frac{w_f(-z_{x,i})}{(\Delta x)^2} \quad \text{and} \quad z_{x,i} = z_2 \quad \text{if } s = 0 \tag{18b}$$

For convenience, the present numerical procedure is summarized as follows.

1. Assume that the free surface profile $h(x, \tau_0)$ and the velocity field (u_0, v_0) at the previous time level $\tau_0 = \tau - \Delta\tau$ are known.
2. Use the method of extrapolated velocity [21,22] to determine the migration velocity of the free surface at the time level τ_0.
3. Estimate the free surface $h(x, \tau)$ for the present time level τ from the migration velocity of the free surface at the previous time level τ_0.
4. Evaluate the curvature κ of the free surface $h(x, \tau)$.
5. Estimate the pressure $\hat{p}_l(x, h, \tau)$ on the liquid side of the free surface from Eq. (14).
6. Based on the pressure $\hat{p}_l(x, h, \tau)$ obtained in Step 5, correct the free surface profile $h(x, \tau)$ with the required dynamic contact angle θ_D.
7. Replace the air velocity (u_0, v_0) with the extrapolated velocity in the narrow layer where the advancing free surface sweeps through during the period from τ_0 to τ.
8. Guess a solution $(u, v, \hat{p})$ for the present time level τ.
9. Solve the momentum Eq. (2) and (3) to renew the velocity (u, v), and then evaluate the migration velocity on the free surface $h(x, \tau)$ with the method of extrapolated velocity [21,22].
10. Use the NAPPLE algorithm [25] to compute the pressure field $\hat{p}_l(x, y, \tau)$ for the liquid based on the free surface pressure $\hat{p}_l(x, h, \tau)$, and compute the pressure field $\hat{p}_a(x, y, \tau)$ for the air based on the migration velocity of the free surface.

11. Return to Step 9 and repeat the computations until the solution $(u, v, \hat{p})$ converges to a prescribed tolerance.
12. Stop the numerical procedure if the prescribed time limit has been reached. Otherwise, set $\tau_0 = \tau$ and $(u_0, v_0, h_0) = (u, v, h)$ then return to Step 3 and repeat the computations for the next time step.

It is noteworthy that the capillary force could have a quite significant effect in the wall region when the surface tension γ is large and the contact angle is close to either 0° or 180°. Moreover, the free surface profile $h(x, \tau)$ estimated in Step 3 does not necessarily satisfy the required dynamic contact angle θ_D on the wall. Hence, the force balance Eq. (14) is solved with the geometry method [26] in Step 6 to correct the free surface profile $h(x, \tau)$ in the wall region $x_{\text{joint}} \leqslant x \leqslant 1$. As illustrated in Fig. 2, the curvature at the joint $\kappa(x_{\text{joint}}, \tau)$ is guessed and adjusted with a shooting method to achieve the required dynamic contact angle $\theta_D(\tau)$, while $h(x_{\text{joint}}, \tau)$, $h'(x_{\text{joint}}, \tau)$ and the pressure distribution $\hat{p}_l(x, h, \tau)$ are all maintained at their original values. Such a strategy is equivalent to introducing a slip boundary condition for the contact line, and thus successfully removes the stress singularity arising from the no-slip condition imposed on the wall ($x = 1$) for both liquid and air regions. However, correction of the free surface profile might influence the mass conservation in the wall region (see Fig. 2). This will be discussed later.

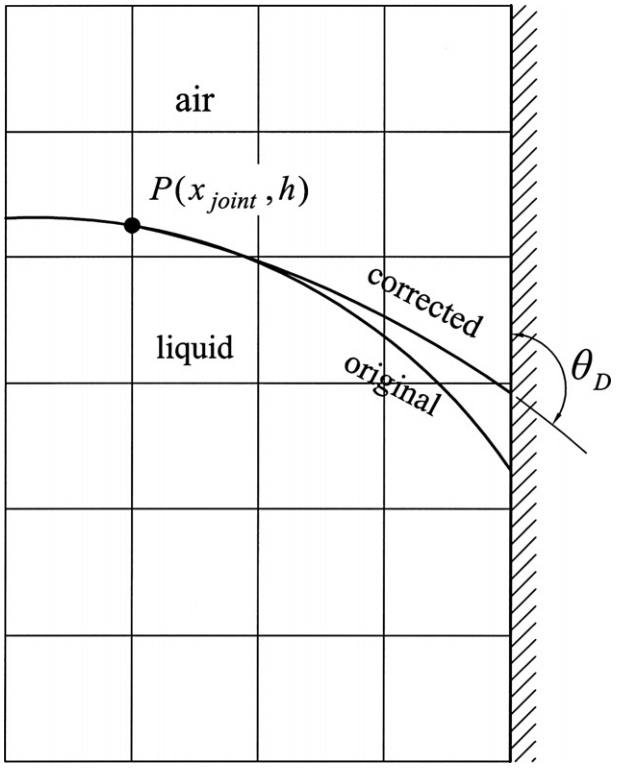

Fig. 2. A schematic representation of free surface correction in the wall region.

4. Evaluation of the curvature

In Step 3 of the numerical procedure described in the previous section, the free surface $h(x, \tau)$ for the present time level τ is estimated from the previous profile $h(x, \tau_0)$ by tracking the markers on it. The spacing between two adjacent markers is $\Delta x/10$ approximately. The resulting free surface having the discrete form $h_i = h(x_i, \tau)$ is interpolated from the markers. However, it is a great difficulty to evaluate the curvature with Eq. (7b) for the discrete function $h(x_i, \tau)$ due to numerical noise. To circumvent the numerical difficulty, the smoothing cubic spline [27] is employed in Step 4. Note that the algorithm described by Lancaster and Salkauskas [27] can be significantly simplified to save the CPU time if performed on a uniform grid system. For convenience, such a simplified version is presented as following.

Let (x_i, y_i), $i = 1, 2 \ldots, n$, be a discrete form of function $y(x)$, where $x_i = (i-1)\Delta x$ is a uniform grid system. In the conventional free cubic spline formulation [28], the function $y(x)$ in the interval $[x_i, x_{i+1}]$ is approximated by a cubic polynomial of the form

$$s(x) = a_i + b_i(x - x_i) + c_i(x - x_i)^2 + d_i(x - x_i)^3 \tag{19}$$

where $s(x)$ represents a piecewise continuous function over the whole domain $x_1 \leqslant x \leqslant x_n$. The second derivatives of the spline function $s(x)$ at the grid points then are determined from

$$\boldsymbol{B}\boldsymbol{s}'' = \boldsymbol{D}\hat{\boldsymbol{y}} \tag{20}$$

where $\boldsymbol{s}'' = \{s_1'', s_2'', \ldots, s_n''\}^{\mathrm{T}}$, $\hat{\boldsymbol{y}} = \{\hat{y}_1, \hat{y}_2, \ldots, \hat{y}_n\}^{\mathrm{T}}$, $s_i'' = s''(x_i) = 2c_i$, $\hat{y}_i = \beta y_i$, $\beta = \frac{6}{(\Delta x)^2}$, and

$$\boldsymbol{B} = \begin{bmatrix} 1 & 0 & 0 & 0 & 0 & 0 & 0 \\ 0 & 4 & 1 & 0 & 0 & 0 & 0 \\ 0 & 1 & 4 & 1 & 0 & 0 & 0 \\ 0 & 0 & 1 & 4 & 1 & 0 & 0 \\ 0 & 0 & 0 & 1 & 4 & 1 & 0 \\ 0 & 0 & 0 & 0 & 1 & 4 & 0 \\ 0 & 0 & 0 & 0 & 0 & 0 & 1 \end{bmatrix}$$

$$\boldsymbol{D} = \begin{bmatrix} 0 & 0 & 0 & 0 & 0 & 0 & 0 \\ 1 & -2 & 1 & 0 & 0 & 0 & 0 \\ 0 & 1 & -2 & 1 & 0 & 0 & 0 \\ 0 & 0 & 1 & -2 & 1 & 0 & 0 \\ 0 & 0 & 0 & 1 & -2 & 1 & 0 \\ 0 & 0 & 0 & 0 & 1 & -2 & 1 \\ 0 & 0 & 0 & 0 & 0 & 0 & 0 \end{bmatrix} \tag{21}$$

Unfortunately, the interpolation function generated by the method of free cubic spline could oscillate wildly if there is a large noise in the original data y_i. This implies the need of filtering the noise. Suppose that the original data y_i becomes s_i, $i = 1, 2, \ldots, n$ after the noise is filtered. Applying the numerical procedure of a standard free cubic spline on s_i, one gets

$$\boldsymbol{B}\boldsymbol{s}'' = \boldsymbol{D}\hat{\boldsymbol{s}} \tag{22}$$

where $\hat{s} = \{\hat{s}_1, \hat{s}_2, \ldots, \hat{s}_n\}^{\mathrm{T}}$ and $\hat{s}_i = \beta s_i$. This gives rise to

$$s''(x) = 2c_i + 6d_i(x - x_i) = s_i'' L_i(x) \tag{23}$$

in the interval $[x_i, x_{i+1}]$, where $s_i' = 2c_i$ and

$$L_i(x) = \begin{cases} 1 + \left(\frac{s_{i+1}''}{s_i''} - 1\right)\left(\frac{x - x_i}{\Delta x}\right) & \text{if } x_i \leqslant x < x_{i+1} \\ 0 & \text{otherwise} \end{cases} \tag{24}$$

is the Lagrange linear interpolation polynomial. Thus, the second derivative of the smoothing cubic spline is expressible as the vector form

$$s''(x) = \sum_{i=1}^{n} s_i'' L_i = (\boldsymbol{s}'')^{\mathrm{T}} \boldsymbol{L} = \boldsymbol{L}^{\mathrm{T}} \boldsymbol{s}'' \tag{25}$$

where $\boldsymbol{L} = \{L_1, L_2, \ldots, L_n\}^{\mathrm{T}}$ is a vector containing the tent functions that are needed to form the piecewise continuous linear function $s''(x)$ for a free cubic spline. Next, define the functional

$$K_\lambda(s) = E(s) + \lambda \Delta x J(s) \tag{26}$$

$$E(s) = \sum_{i=1}^{n} (s_i - y_i)^2 \quad \text{and} \quad J(s) = \int_{x_1}^{x_n} (s''(x))^2 \, \mathrm{d}x \tag{27}$$

where λ is a prescribed nonnegative constant ($\lambda \geqslant 0$). In vector form

$$E(s) = \sum_{i=1}^{n} (s_i - y_i)^2 = (\boldsymbol{s} - \boldsymbol{y})^{\mathrm{T}} (\boldsymbol{s} - \boldsymbol{y}) \tag{28}$$

$$\begin{aligned} J(s) &= \int_{x_1}^{x_n} (s''(x))^2 \, \mathrm{d}x = \int_{x_1}^{x_n} (\boldsymbol{s}')^{\boldsymbol{T}} \boldsymbol{L}\boldsymbol{L}^{\boldsymbol{T}} \boldsymbol{s}'' \, \mathrm{d}x \\ &= (\boldsymbol{s}'')^{\boldsymbol{T}} \left(\int_{x_1}^{x_n} \boldsymbol{L}\boldsymbol{L}^{\boldsymbol{T}} \, \mathrm{d}x \right) \boldsymbol{s}'' = \frac{1}{\beta \Delta x} (\boldsymbol{s}')^{\mathrm{T}} \boldsymbol{B}\boldsymbol{s}'' \end{aligned} \tag{29}$$

Substituting the second derivative (22)

$$\boldsymbol{s}'' = \boldsymbol{B}^{-1}\boldsymbol{D}\hat{\boldsymbol{s}} \quad \text{or} \quad (\boldsymbol{s}'')^{\mathrm{T}} = (\hat{\boldsymbol{s}})^{\mathrm{T}} D^{\mathrm{T}} (\boldsymbol{B}^{-1})^{\mathrm{T}} \tag{30}$$

into Eq. (29) and noting that $\boldsymbol{B}$ is a symmetric matrix, one has

$$J(s) = \frac{1}{\beta \Delta x} (\hat{\boldsymbol{s}})^{\mathrm{T}} \boldsymbol{D}^{\mathrm{T}} \boldsymbol{B}^{-1} \boldsymbol{B} \boldsymbol{B}^{-1} \boldsymbol{D}\hat{\boldsymbol{s}} = \frac{1}{\Delta x} \boldsymbol{s}^{\mathrm{T}} \boldsymbol{D}^{\mathrm{T}} \boldsymbol{B}^{-1} \boldsymbol{D}\hat{\boldsymbol{s}} \tag{31}$$

Thus, the functional can be rewritten as

$$K_\lambda(s) = (\boldsymbol{s} - \boldsymbol{y})^{\mathrm{T}} (\boldsymbol{s} - \boldsymbol{y}) + \lambda \boldsymbol{s}^{\mathrm{T}} \boldsymbol{D}^{\mathrm{T}} \boldsymbol{B}^{-1} \boldsymbol{D}\hat{\boldsymbol{s}} \tag{32}$$

The next step is to find the vector $\boldsymbol{s} = \{s_1, s_2, \ldots, s_n\}^{\mathrm{T}}$ such that the functional reaches a minimum. This can be implemented by differentiating the functional with respect to s_i to yield the necessary condition

$$(\boldsymbol{s} - \boldsymbol{y}) + \lambda \boldsymbol{D}^{\mathrm{T}} \boldsymbol{B}^{-1} \boldsymbol{D}\hat{\boldsymbol{s}} = 0 \tag{33}$$

Multiplying Eq. (33) on the left by $\beta \boldsymbol{D}$ and then replace $D\hat{\boldsymbol{s}}$ by $\boldsymbol{B}\boldsymbol{s}''$, one gets

$$(\boldsymbol{B} + \lambda \beta \boldsymbol{G}) \boldsymbol{s}'' = \boldsymbol{D}\hat{\boldsymbol{y}} \tag{34}$$

where

$$\boldsymbol{G} = \boldsymbol{D}\boldsymbol{D}^{\mathrm{T}} = \begin{bmatrix} 0 & 0 & 0 & 0 & 0 & 0 & 0 \\ 0 & 6 & -4 & 1 & 0 & 0 & 0 \\ 0 & -4 & 6 & -4 & 1 & 0 & 0 \\ 0 & 1 & -4 & 6 & -4 & 1 & 0 \\ 0 & 0 & 1 & -4 & 6 & -4 & 0 \\ 0 & 0 & 0 & 1 & -4 & 6 & 0 \\ 0 & 0 & 0 & 0 & 0 & 0 & 0 \end{bmatrix} \tag{35}$$

Finally, substitute Eq. (30) into Eq. (33) to yield

$$\boldsymbol{s} = \boldsymbol{y} - \lambda \boldsymbol{D}^{\mathrm{T}} \boldsymbol{s}'' \tag{36}$$

This produces a smoothing spline (x_i, s_i) over the original data (x_i, y_i), once the vector $\boldsymbol{s}''$ is determined from Eq. (34).

It is interesting to note that when $\lambda = 0$ is assigned, the principle of minimum functional (27) leads to $s_i = y_i$ and $K_\lambda(s) = 0$, and thus $s(x)$ reduces to the conventional free cubic spline as observable from Eqs. (34) and (36). On the other hand, if λ is large, the minimization of $K_\lambda(s)$ should be close to a least squares straight-line approximation to the data. A straight line has zero second derivative and hence zero $J(s)$. Therefore, $s(x)$ shifts continuously from the conventional free cubic spline to a least squares straight-line approximation when λ gradually increases from zero to infinity. Generally speaking, large λ implies a less sinuous curve, while small λ means a less deviation from the original data. The optimum value for λ, however, is strongly problem-dependent. One should experiment with the value of λ until a satisfactory fit is obtained.

5. Results and discussion

As in the experiment of Coyle et al. [20], silicon oil and air are adopted as the media of the fountain flow in the present study. The physical properties at 25 °C are

$$\begin{aligned} &\rho_{\mathrm{l}} = 970 \text{ kg/m}^3, \quad \mu_{\mathrm{l}} = 52.5 \text{ N s/m}^2 \\ &\rho_{\mathrm{a}} = 1.205 \text{ kg/m}^3, \quad \mu_{\mathrm{a}} = 1.81 \times 10^{-5} \text{ N s/m}^2 \\ &\gamma = 0.021 \text{ N/m} \end{aligned} \tag{37}$$

The corresponding dimensionless parameters are

$$\begin{aligned} &\rho_{\mathrm{a}}/\rho_{\mathrm{l}} = 0.001242, \quad \mu_{\mathrm{a}}/\mu_{\mathrm{l}} = 3.448 \times 10^{-7} \\ &Re = 7.02 \times 10^{-4}, \quad Ca = 5, \quad Bo = 163.3 \end{aligned} \tag{38}$$

based on the gravity $g = 9.806 \text{ m/s}^2$ and the characteristic quantities $L = 0.019$ m and $U_c = 0.002$ m/s. The numerical procedure starts from a made-up initial condition and then marches on a virtual time coordinate until the steady-state solution is reached. When the steady-state flow is reached, the contact line gains an upward "slipping velocity" that equals to V_{wall}. The corresponding capillary number $Ca = 5$ implies a dynamic contact angle of $\theta_{\mathrm{D}} = 176.7°$ based on Hoffman–Kistler's model [29].

Three liquid volumes are employed to examine the influence of the piston. Their corresponding mean liquid depths

are 0.87, 1.95, and 3.95. For convenience, the three cases are referred to as Case 1, Case 2, and Case 3, respectively. After a series of grid tests, the uniform square grid mesh $\Delta x = \Delta y = 0.02$ with $\Delta\tau = 0.001$ is found adequate for all of the three cases. The successive-over-relaxation factors (SOR) employed for the computation are 0.6 and 0.03 for the velocity and the pressure, respectively. The computation for each time step is terminated when both criterions

$$\operatorname{Max}_k \left| \phi_k^{(r)} - \phi_k^{(r-1)} \right| < 10^{-5} \tag{39a}$$

$$\operatorname{Max}_k \left| \frac{\hat{p}_k^{(r)} - \hat{p}_k^{(r-1)}}{\hat{p}_{\max} - \hat{p}_{\min}} \right| < 10^{-4} \tag{39b}$$

are satisfied, where ϕ denotes the velocity components (u and v), and $\phi_k^{(r)}$ is the result of the kth grid point at the rth iteration.

Fig. 3 shows the influence of λ on the resulting free surface curvature obtained by using the smoothing cubic spline method for Case 2. The curvature obtained from Eq. (7b) with the central difference scheme is also plotted in Fig. 3 as a reference (see the dotted curve). Based on the finding from Fig. 3, $\lambda = 0.01$ is adopted to evaluate the curvature of the free surface. Once the curvature is known, the free surface profile in the wall region ($x_{\text{joint}} \leqslant x \leqslant 1$) is corrected with the geometry method [26] to achieve the desired dynamic contact angle ($\theta_D = 176.7^\circ$) on the contact line. Influence of x_{joint} is examined in Fig. 4 through three x_{joint} values for Case 2. From Fig. 4, the value of x_{joint} is seen to have only a negligible influence on the free surface profile $h(x, \infty)$. Hence, the free surface profile is corrected only in the region $0.9 \leqslant x \leqslant 1$ for simplicity. At very beginning of the numerical procedure ($\tau \approx 0$), correction of the free surface profile is quite

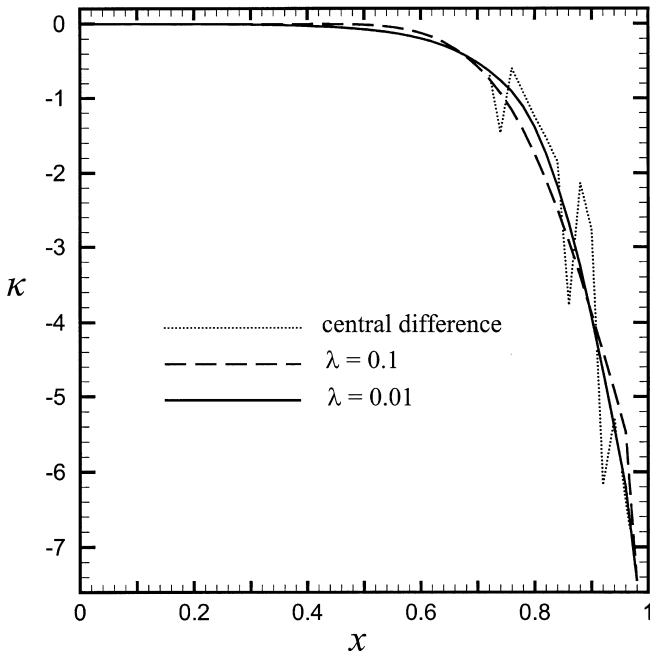

Fig. 3. Influence of λ on the curvature in smoothing cubic spline.

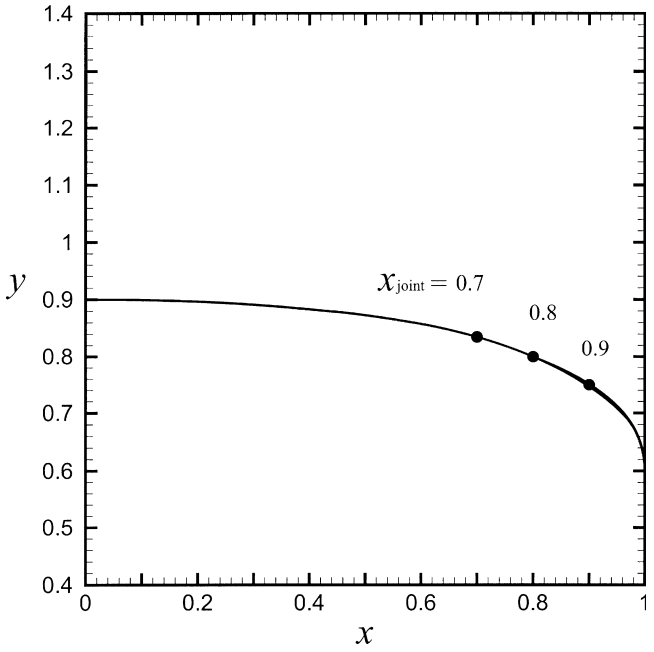

Fig. 4. Influence of x_{joint} on the free surface for Case 2.

significant due to the fact that the "initial" free surface profile $h(x, 0)$ has an "incorrect" contact angle $\theta_D = 90^\circ$. This implies the need of correcting the overall mass conservation. Fortunately, the correction becomes negligibly small when the virtual time τ is sufficiently large.

In the present study, the primary variables $(u, v, \hat{p})$ are solved directly from the governing equations. For a clear observation on the flow pattern, the stream function is evaluated from

$$\psi = -\int_0^x v \, dx \tag{40}$$

once the velocity is available. The integration (40) can be performed across the free surface because the continuity Eq. (1) is valid in both liquid and air regions despite of the great density difference. Fig. 5 reveals the streamlines $\psi = constant$ and the isobars $\hat{p} = constant$ for the steady-state solution of Case 1. The increments are 0.02 and 1 for the streamlines and the isobars, respectively. The bold-face curve represents the free surface. It is important to note that the stream function is negative in both liquid and air regions, while the maximum 0.003 occurs in a narrow "positive region" adjacent to the free surface. This evidences that the toroidal-like motion postulated by Dussan V. [13] exists even in the liquid–air system.

It can be verified from the momentum equation (2) and (3) that the pressure $\hat{p}$ is constant in static fluids ($u = v = 0$). Thus, the variation of $\hat{p}$ in Fig. 5 is induced by the fluid flow. Due to the small density and viscosity, the flow-induced pressure $\hat{p}_a$ in the air is essentially zero (less than 0.5) as observable from Fig. 5. Use of the boundary condition $\partial v(x, 5, \tau)/\partial y = 0$ in Eq. (10) is only for numerical convenience. The numerical result for the liquid

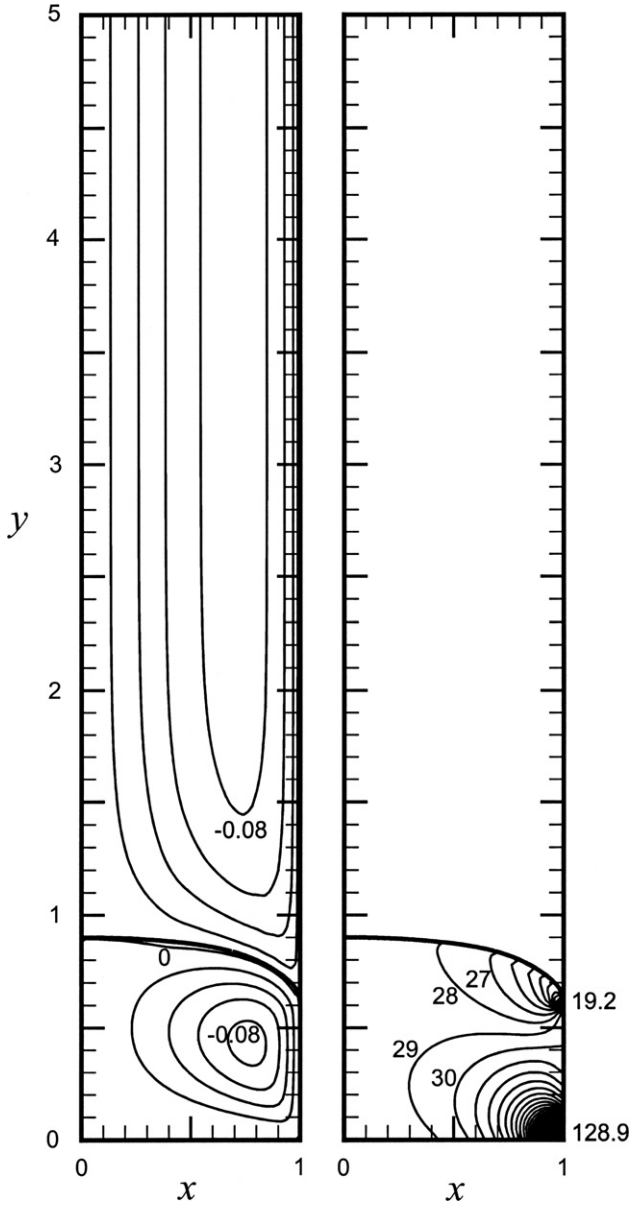

Fig. 5. Streamlines with increment $\Delta\psi = 0.02$ and isobars with increment $\Delta\hat{p} = 1$ for Case 1.

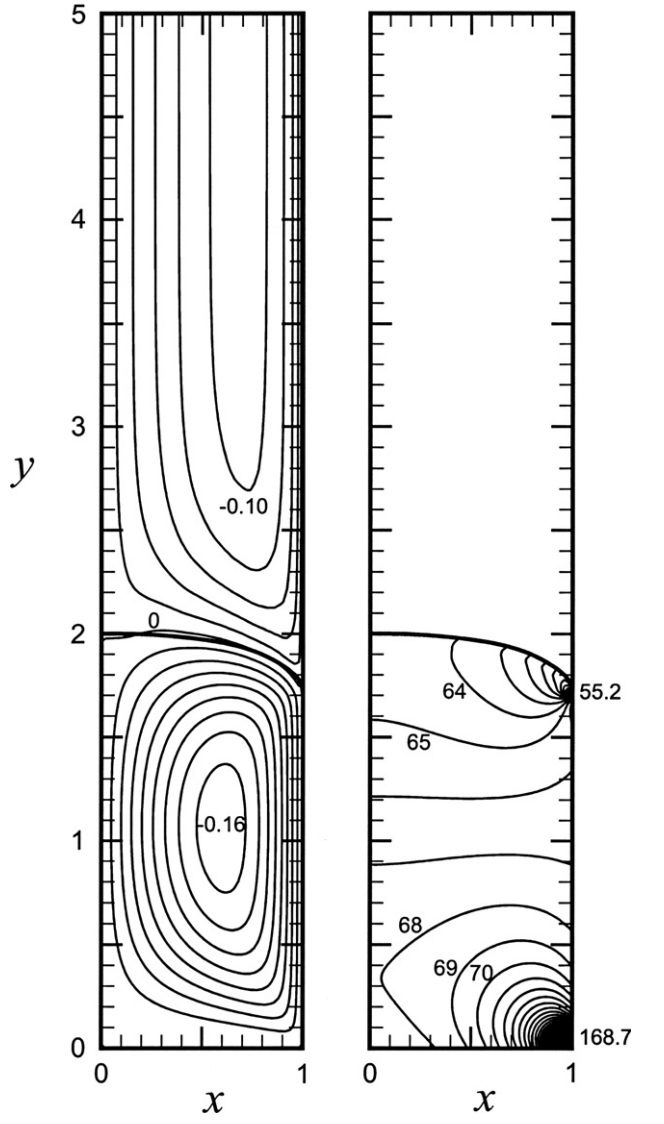

Fig. 6. Streamlines with increment $\Delta\psi = 0.02$ and isobars with increment $\Delta\hat{p} = 1$ for Case 2.

region and the free surface would not be significantly influenced if the boundary condition $v(x, 5) = 0$ is used instead.

The flow pattern and the pressure field in the liquid region of Fig. 5 is similar to that of the classic lid-driven flow on a square cavity [25]. Along the free surface, the pressure $\hat{p}_l$ is seen to decrease from 28.3 in the centerline to 19.2 on the sleeve wall, while the air pressure essentially maintains at $\hat{p}_a \approx 0.5$. The pressure gradient offers a driven force for the liquid to move along the free surface from the centerline to the wall. It could be a good measure for the strength of the fountain flow. The minimum pressure occurring at the contact line can be attributed to the "slipping free surface" on the sleeve wall. Such a "suction force" comes mainly from the body force *Boh* because a large Bond number ($Bo = 163.3$) occurs in the present case (see Eq. (14)). This evidences the importance of the capillary force (surface tension plus contact angle) that determines the free surface profile $h(x, \tau)$ in the wall region. Similar situations are found in Figs. 6 and 7 for Case 2 and Case 3, respectively. In their study on a fountain flow problem for viscoelastic fluids, Sato and Richardson [30] neglected the capillary force, and thus did not observe the "suction force" at the contact line.

The isobars shown in Fig. 7 clearly distinguish three regions of flow, i.e. a fountain flow just behind the free surface, a plane shear flow behind the fountain flow ($1 < y < 3$), and a recirculation flow near the piston. The pressure gradient is essentially constant in the plane shear flow region. This same feature occurs also in the fountain flow problem for viscoelastic fluids [30]. From Figs. 5–7, it is seen that the plane shear flow region shrinks when the liquid volume decreases. It could even entirely disappear when the liquid volume is small (see Fig. 5 for instance).

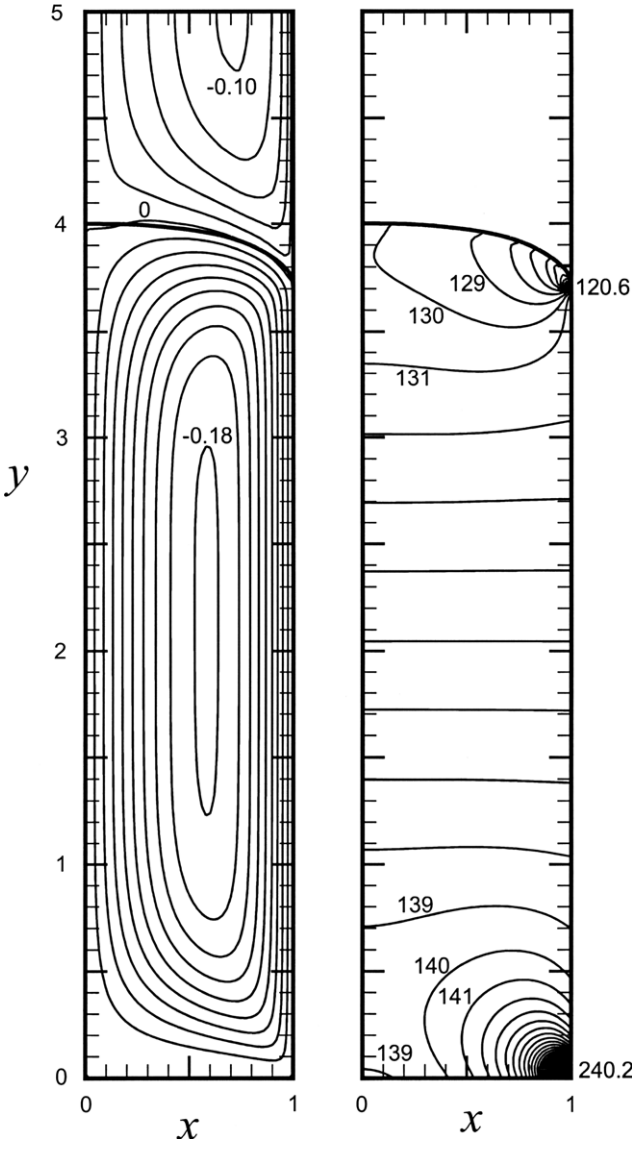

Fig. 7. Streamlines with increment $\Delta\psi = 0.02$ and isobars with increment $\Delta\hat{p} = 1$ for Case 3.

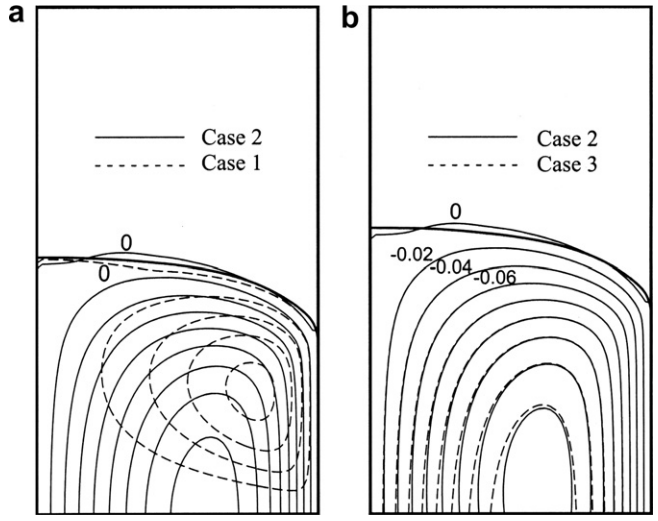

Fig. 8. Comparisons of streamlines and free surface among Case 1, 2, and 3.

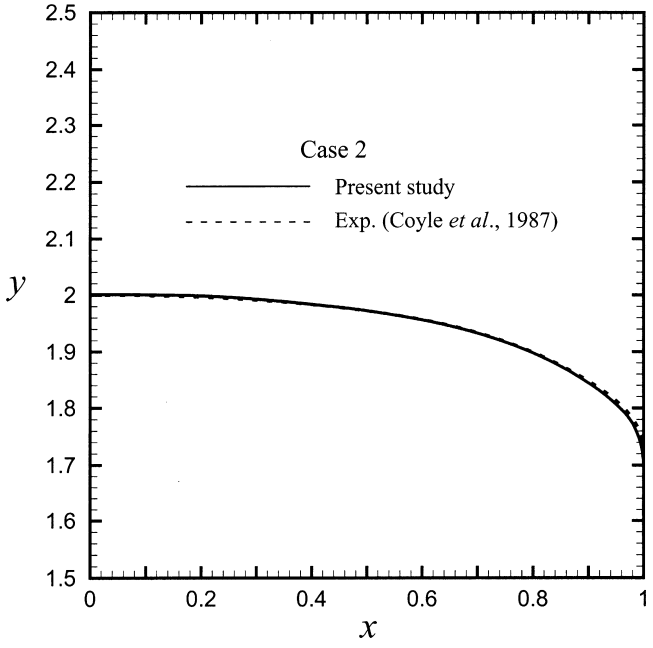

Fig. 9. Comparison of free surface between present prediction and experiment.

Fig. 8 shows comparisons among Case 1, Case 2, and Case 3 for the effect of the liquid volume on the streamlines in the fountain flow region. The effect of the liquid volume on the free surface profile is negligible such that the free surface profiles of the three cases can be represented by a single bold-face curve. Fig. 8b reveals that the streamlines are not influenced by the liquid volume as long as the liquid volume is sufficiently large. Surprisingly, however, the great difference between the streamlines of Case 1 and Case 2 in Fig. 8a has no effect on the free surface profile. To examine the accuracy of the present numerical results, the free surface profile obtained in Case 2 is compared with an experimental observation traced from the photograph of Coyle et al. [20] under the same conditions. Excellent agreement between the present prediction and the experimental data can be observed from Fig. 9.

Finally, the velocity profile $v(x,y)$ is examined in Figs. 10–12 for Case 1, Case 2, and Case 3, respectively. Fig. 10a depicts that the velocity is zero on the top of the aluminum piston $y = 0$. Due to the no-slip condition on the sleeve wall, the velocity in the wall region becomes negative at $y > 0$. This induces an accelerating flow in the core region for the law of mass conservation. The maximum velocity occurs at a point near $(x,y) = (0.6, 0.5)$. As observable from Fig. 10, the velocity at the centerline increases from zero at $y = 0$ to 0.081 at $y = 0.5$, and then decreases to zero on the free surface at $y = 0.9$ (Note that the velocity profile at $y = 0.9$ is not shown here because it is entirely in the air region except for the point $x = 0$.). This is the characteristic of a fountain flow. Similar phenomenon can be

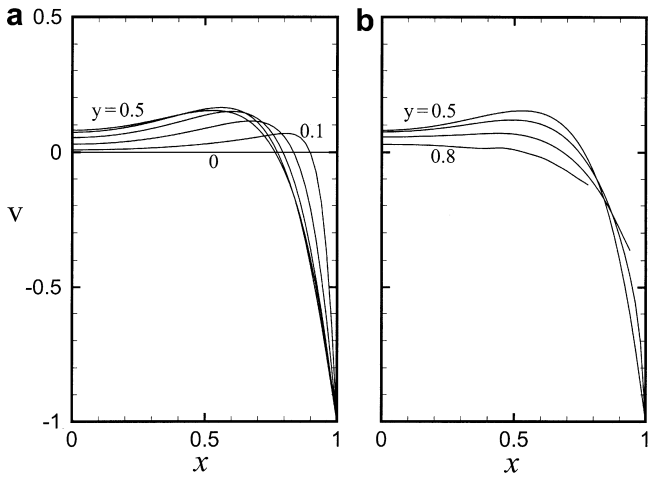

Fig. 10. Velocity profile $v(x, y, \infty)$ for Case 1.

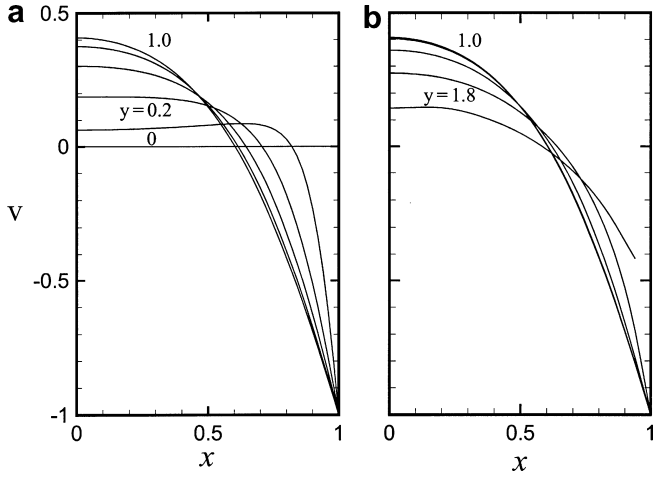

Fig. 11. Velocity profile $v(x, y, \infty)$ for Case 2.

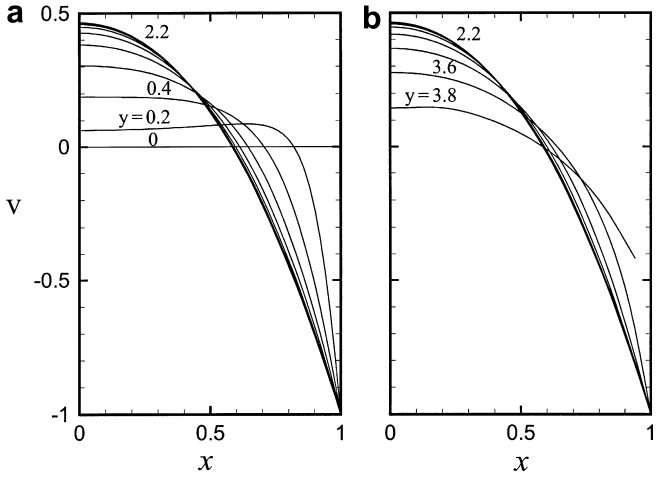

Fig. 12. Velocity profile $v(x, y, \infty)$ for Case 3.

found in Figs. 11 and 12 for the cases of larger liquid volume. The major difference between Case 1 and Case 3 is that there is a parabolic velocity profile in Case 3 before the fountain flow region is reached.

In the liquid–gas system, the great density and viscosity jumps across the free surface give rise to a great pressure jump (8). Instead of imposing the pressure jump on the free surface, the front-tracking method [31–33] formulates the surface tension with a source term of integral form in the momentum equation. In the numerical implementation, however, the free surface is smeared into a finite thickness such that both density and viscosity "gradients" exist across the free surface. The quantities on the free surface are transferred to the nearest grid points. Such a treatment could generate anisotropic surface tension force and thus wiggling pressure and unphysical velocity (parasitic current) on the free surface, especially when the surface tension force is large [32,33]. As remarked by Tryggvason et al. [32], small error can lead to negative densities that usually cause convergence difficulties when the density ratio is large. This implies that the continuity Eq. (1) across the free surface is not precisely satisfied in the front-tracking method [31–33]. Similar numerical difficulties occur in the use of the level set method [34]. In the present study, the density and viscosity jumps are properly handled with the integration scheme (see Eq. (15)), while the pressure jump (8) is imposed exactly on the free surface through the use of the NAPPLE algorithm. Hence, the numerical difficulties encountered in the previous works [32–34] do not occur in the present study. Moreover, the advancement of the free surface is usually restricted to less than one grid mesh in the front-tracking method [32]. Use of the present numerical method has no such a limitation.

As a final note it is mentioned that a smooth-looking curve could have a wildly oscillating curvature profile (see Figs. 4 and 3 for instance) if the curvature is evaluated from Eq. (7b) without a proper treatment. Computing the curvature of a three-dimensional curvilinear surface is even more difficult. This is the major numerical difficulty in fluid flow problems dealing with a very strong capillary force (surface tension force). The ghost fluid method [35,36] and the hybrid particle level set method [37] were reported to capture the free surface with only little numerical diffusion. However, the capillary force that prevails in the wall region is not investigated in the works [35–37]. In the present study, the geometry method [26] along with the smoothing cubic spline [27] is adopted to handle the capillary force with a great success. Unfortunately, the proposed method is valid only for two-dimensional and axisymmetric problems. Their counterparts in the three-dimensional problems are needed.

6. Conclusion

A fountain flow in a liquid–air system is studied in the paper. A single set of governing equations over the entire physical domain including the liquid, the air, and the free surface is solved with the extended weighting function scheme and the NAPPLE algorithm on a fixed Cartesian grid system. The result reveals that there is a toroidal-like motion on the free surface even in liquid–air system. This

is consistent with the theory of the viscous flow. The piston is found to have no influence on the free surface profile as long as the distance between the free surface and the piston is larger than the width of the fountain flow. The capillary force (surface tension plus contact angle) has a dominate effect on the shape of the liquid meniscus in the wall region. To ensure the required dynamic contact angle, the free surface profile in the wall region is corrected by solving the nonlinear force balance equation with the geometry method. This is equivalent to introducing a slip condition at the contact line, and thus successfully circumvents the stress singularity. The strategy is equally applicable for three-dimensional problems in case a particular numerical method is available that solves the force balance equation to yield a three-dimensional meniscus shape adjacent to the contact line.

Acknowledgement

The authors wish to express their appreciation to the National Science Council of Taiwan for the financial support of this work through the contract NSC 92-2212-E007-017.

References

[1] W. Rose, Fluid–fluid interfaces in steady motion, Nature 191 (1961) 242–243.
[2] E.B. Dussan V., S.H. Davis, On the motion of a fluid–fluid interface along a solid surface, J. Fluid Mech. 65 (1974) 71–95.
[3] E.B. Dussan V., The moving contact line: the slip boundary condition, J. Fluid Mech. 77 (1976) 665–684.
[4] R.G. Cox, Inertial and viscous effects on dynamic contact angle, J. Fluid Mech. 357 (1998) 249–278.
[5] J. Koplik, J.R. Banavar, J.F. Willemsen, Molecular dynamics of Poiseuille flow and moving contact line, Phys. Rev. Lett. 60 (1988) 1282–1285.
[6] P.A. Thompson, M.O. Robbins, Simulations of contact-line: slip and the dynamic contact angle, Phys. Rev. Lett. 63 (1989) 766–769.
[7] K.M. Jansons, Moving contact lines on a two-dimensional rough surface, J. Fluid Mech. 154 (1985) 1–28.
[8] K.M. Jansons, Moving contact lines at non-zero capillary number, J. Fluid Mech. 167 (1986) 393–407.
[9] R.A. Behrens, M.J. Crochet, C.D. Denson, A.B. Metzner, Transient free-surface flows: motion of a fluid advancing in a tube, AIChE J. 33 (1987) 1178–1186.
[10] J.M. Kim, K.H. Ahn, S.J. Lee, S.J. Lee, Numerical simulation of moving free surface problems in polymer procession using volume-of-fluid method, Polym. Eng. Sci. 41 (2001) 858–866.
[11] H. Mavridis, A.N. Hrymak, J. Vlachopoulos, Transient free-surface flows in injection model filling, AIChE J. 34 (1988) 403–410.
[12] R.L. Hoffman, A study of the advancing interface I. Interface shape in liquid–gas systems, J. Colloid Interface Sci. 50 (1975) 228–241.
[13] E.B. Dussan V., Immiscible liquid displacement in a capillary tube: the moving contact line, AIChE J. 23 (1977) 131–133.
[14] M.R. Kamal, E. Chu, P.G. Lafleur, Computer simulation of injection mold filling for viscoelastic melts with fountain flow, Polym. Eng. Sci. 26 (1986) 190–196.
[15] H. Mavridis, A. Hrymak, J. Vlachopoulos, Finite element simulation of fountain flow in injection molding, Polym. Eng. Sci. 26 (1986) 449–454.
[16] C.G. Gogos, C.F. Huang, The process of cavity filling including the fountain flow in injection molding, Polym. Eng. Sci. 26 (1986) 1457–1466.
[17] M.R. Kamal, S.K. Goyal, E. Chu, Simulation of injection mold filling of viscoelastic polymer with fountain flow, AIChE J. 34 (1988) 94–106.
[18] X. Jin, Boundary element study on particle orientation caused by the fountain flow in injection molding, Polym. Eng. Sci. 33 (1993) 1238–1242.
[19] H.-S. Lee, Finite element analysis for the flow characteristics along the thickness direction in injection molding, Polym. Eng. Sci. 37 (1997) 559–567.
[20] D.J. Coyle, J.W. Blake, C.W. Macosko, The kinematics of fountain flow in mold-filling, AIChE J. 33 (1987) 1168–1177.
[21] S.L. Lee, S.R. Sheu, A new numerical formulation for incompressible viscous free surface flow without smearing the free surface, Int. J. Heat Mass Transfer 44 (2001) 1837–1848.
[22] S.L. Lee, S.R. Sheu, Filling process in an open tank, ASME J. Fluids Eng. 125 (2003) 1016–1021.
[23] S.L. Lee, Weighting function scheme and its application on multidimensional conservation equations, Int. J. Heat Mass Transfer 32 (1989) 2065–2073.
[24] S.L. Lee, R.Y. Tzong, An enthalpy formulation for phase change problems, Int. J. Heat Mass Transfer 34 (1991) 1491–1502.
[25] S.L. Lee, R.Y. Tzong, Artificial pressure for pressure-linked equation, Int. J. Heat Mass Transfer 35 (1992) 2705–2716.
[26] S.L. Lee, H.D. Lee, Evolution of liquid meniscus shape in a capillary tube, ASME J. Fluids Eng. 129 (2007) 957–965.
[27] P. Lancaster, K. Salkauskas, Curve and Surface Fitting: An Introduction, Academic Press, London, 1986, pp. 101–111.
[28] R.L. Burden, J.D. Faires, Numerical Analysis, seventh ed., Brook/Cole Publishing, Pacific Grove, California, 2001, pp. 141–146.
[29] S.F. Kistler, Hydrodynamics of wetting, in: J.C. Berg (Ed.), Wettability, Marcel Dekker, New York, 1993, pp. 311–429.
[30] T. Sato, S.M. Richardson, Numerical simulation of the fountain flow problem for viscoelastic fluids, Polym. Eng. Sci. 35 (1995) 805–812.
[31] S.O. Unverdi, G. Tryggvason, A front-tracking method for viscous, incompressible, multi-fluid flows, J. Comput. Phys. 100 (1992) 25–37.
[32] G. Tryggvason, B. Bunner, A. Esmaeeli, D. Juric, N. Al-Rawahi, W. Tauber, J. Han, S. Nas, Y.-J. Jan, A front-tracking method for the computations of multiphase flow, J. Comput. Phys. 169 (2001) 708–759.
[33] S. Shin, D. Juric, Modeling three-dimensional multiphase flow using a level contour reconstruction method for front tracking without connectivity, J. Comput. Phys. 180 (2002) 427–470.
[34] H. Takahira, T. Horiuchi, S. Banerjee, An improved three-dimensional level set method for gas–liquid two-phase flows, ASME J. Fluids Eng. 126 (2004) 578–585.
[35] R.P. Fedkiw, T. Aslam, B. Merriman, S. Osher, A non-oscillatory Eulerian approach to interface in multimaterial flows (the ghost fluid method), J. Comput. Phys. 152 (1999) 457–492.
[36] R.P. Fedkiw, T. Aslam, S. Xu, The ghost fluid method for deflagration and detonation discontinuities, J. Comput. Phys. 154 (1999) 393–427.
[37] D. Enright, R. Fedkiw, J. Ferziger, I. Mitchell, A hybrid particle level set method for improved interface capturing, J. Comput. Phys. 183 (2002) 83–116.